HHS Public Access

Author manuscript

IEEE Access. Author manuscript; available in PMC 2024 August 29.

Published in final edited form as:

IEEE Access. 2024 ; 12: 20962–20972. doi:10.1109/access.2024.3357355.

Deep Filtered Back Projection for CT Reconstruction

XI TAN[1], **XUAN LIU**[2], **KAI XIANG**[2], **JING WANG**[3], **SHAN TAN**[2]

[1]College of Electrical and Information Engineering, Hunan University of Technology, Zhuzhou 80305, China

[2]School of Artificial Intelligence and Automation, Huazhong University of Science and Technology, Wuhan 430074, China

[3]Department of Radiation Oncology, University of Texas Southwestern Medical Center, Dallas, TX 75390, USA

Abstract

Filtered back projection (FBP) is a classic analytical algorithm for computed tomography (CT) reconstruction, with high computational efficiency. However, images reconstructed by FBP often suffer from excessive noise and artifacts. The original FBP algorithm uses a window function to smooth signals and a linear interpolation to estimate projection values at un-sampled locations. In this study, we propose a novel framework named DeepFBP in which an optimized filter and an optimized nonlinear interpolation operator are learned with neural networks. Specifically, the learned filter can be considered as the product of an optimized window function and the ramp filter, and the learned interpolation can be considered as an optimized way to utilize projection information of nearby locations through nonlinear combination. The proposed method remains the high computational efficiency of the original FBP and achieves much better reconstruction quality at different noise levels. It also outperforms the TV-based statistical iterative algorithm, with computational time being reduced in an order of two, and state-of-the-art post-processing deep learning methods that have deeper and more complicated network structures.

Keywords

Analytical reconstruction; deep learning; FBP; neural network

I. INTRODUCTION

X-RAY computed tomography (CT) is an important tool for non-invasive diagnoses in modern medicine. However, repeated exposure to CT scanning may increase the risk of cancer and some other diseases like genetic defects [1]. Decreasing tube current and exposure time is one of the most practical ways to decrease radiation dose. However, low-dose CT imaging with classic methods such as FBP may lead to excessive noise and artifacts in reconstructed images, which could affect diagnoses [2].

Corresponding author: Shan Tan (shantan@hust.edu.cn).

Several improved FBP algorithms have been proposed to deal with low-dose CT reconstruction. Zhong, et al. improved the filtered back-projection with wavelet denoising [3]. Nielsen et al. calculated a filter matrix which was multiplied with the projection data to improve the reconstruction performance [4]. Qu et al. applied a mean filter on the projection domain before performing the filtered back-projection [5]. Pelt and Batenburg used a customized data-dependent filter that minimizes the projection error of reconstructed images [6]. Mu and Park optimized the filter to suppress image artifacts in MR-FBP [7].

Iterative algorithms have been widely explored to improve the image reconstruction quality of low-dose CT. There are two categories of iterative reconstruction algorithms: algebraic-based ones and statistics-based ones. Algebraic-based algorithms directly relate an image to its projections by linear equations that are solved iteratively to achieve reconstruction. There are many variants, including the algebraic reconstruction technique (ART) [8], simultaneous iterative reconstruction technique (SIRT) [9], and simultaneous algebraic reconstruction technique (SART) [10]. Statistical iterative reconstruction (SIR) algorithms achieve reconstruction by optimizing target functions in which prior information is expressed through regularization terms. SIR algorithms have shown better performance than FBP and algebraic-based iterative algorithms. Different regularization terms have been designed for noise reduction and information preservation [11], [12], [13], [14], [15], [16]. However, SIR algorithms are time-consuming due to their large number of iterations.

Deep learning has achieved great success in medical imaging. The most popular way is to use deep learning as a post-processing procedure that suppresses noise and artifacts in images reconstructed by traditional methods such as FBP [17], [18], [19]. For example, Chen et al. [18] used REDCNN [17], and Wu et al. [19] used an improved DnCNN [20], both to suppress noises on reconstructed CT images. Other post-processing algorithms may use the perceptual loss [21], [22], generative adversarial networks (GAN) [24], [25], and multiple CT image layers information [23]. Although these post-processing algorithms have shown promising results, they do not really take the image reconstruction process into account. In contrast, some researchers combined deep learning with SIR for reconstruction. Alder et al. used the PrimalDual Hybrid Gradient (PDHG) optimization algorithm to expand the statistical iterative target function and replaced the proximal operators with convolutional neural networks [26]. Wu et al. combined the K-Sparse Auto-encoder network with the separable quadratic surrogate algorithm for iterative reconstruction [27]. Chen et al. used the half quadratic splitting (HQS) technique and the Gauss-Seidel method for CBCT reconstruction [28].

In addition to its application in post-processing and iterative reconstruction, deep learning has also been combined with FBP directly. Syben et al. learned a diagonal matrix representing the filter in the frequency domain [29]. Würfl et al. used a convolution operation corresponding to the filter operation and represented the back projection as a fully connected layer [30]. He et al. used a learnable fully-connected filtering layer, a learnable sinusoidal back-projection layer, and a common neural network for reconstruction [31].

In this study, we propose a new FBP framework combined with deep learning, termed DeepFBP, which can obtain high-quality reconstructed images while still retaining the

computational advantage of the original FBP. The proposed DeepFBP framework consists of two key components: a learnable window function and a learnable interpolation operator. Our contributions can be summarized as follows:

A. TO LEARN A DATA-DRIVEN WINDOW FUNCTION

Filtering in the projection domain is one of the most important operations in FBP, in which a classical window function, such as the Rectangular window [32], the Hamming window [33], the Hann window [34], the Cosine window [35], or the Sine window [36], is manually selected for the reconstruction. Sophisticated window function has also been developed and shown improved performance in CT reconstruction. For example, Yu et al. applied the Parzen window in the filtered back-projection algorithm [37]. Farquhar et al. investigated a methodology for informed selection of the filter function and the cut-off frequency for FBP [38]. Zeng et al. derived a ray-by-ray weighted filtered back projection (rFBP) algorithm [39]. Zeng also developed a modified window function so that the analytical FBP algorithm behaved as an iterative Landweber algorithm [40]. Generally speaking, a window function or filter in these studies was designed to achieve a balance between noise suppression and resolution preservation. Different from existing studies, we design a neural network to implicitly learn an optimized window function for FBP in this study. In our experiments, the learned window function leads to excellent performance for FBP reconstruction. Besides, the computational complexity of the learned filters is nearly the same as the original one, without bringing any additional computing time.

B. TO LEARN A DATA-DRIVEN NONLINEAR INTERPOLATION OPERATOR

The interpolation operator during back-projection plays an important role in FBP [41]. The linear interpolation is a popular selection in the traditional FBP algorithm. Note that linear interpolation is vulnerable to noise, and may lead to information loss in the process of back-projection [42]. Different interpolation methods have been proposed for FBP. Horbelt et al. considered using spline interpolation to improve the standard FBP reconstruction [43]. Schaller et al. presented a spiral interpolation approach for multislice spiral computed tomography [44]. McCann proposed to use a cost-efficient pre-filter method for CT reconstruction [45]. In this study, we propose an interpolation operator learned using neural networks. This new interpolation method can utilize more information from nearby detector bins. The parameters of interpolation are learned from a large training dataset automatically. The operator can not only take full advantage of the nearby bins but also avoid manual parameter selection. In this way, we achieve a data-dependent interpolation that fits a specific task better. We explore both the learnable linear and non-linear interpolation operators. Both have much better performance than traditional interpolation, and the nonlinear one performs the best in our experiments.

II. METHODS

Let $f(x, y)$ denote a 2D image and $p(r, \theta)$ the line integral of the image over the line $r = x\,cos\theta + y\sin\theta$. The classical FBP algorithm includes two steps. The first step is a filtering operation over the projection data at each angle:

$$Q(\omega,\theta) = P(\omega,\theta)|\omega|, \tag{1}$$

where $P(\omega,\theta)$ denotes the Fourier transform of the projection $p(r,\theta)$, and $|\omega|$ is a ramp filter. The second step is back-projection, which calculates $q(r,\theta)$ from $Q(\omega,\theta)$ through the inverse Fourier transform, and reconstructs the original image $f(x,y)$ using the back-projection operation over $q(r,\theta)$:

$$f(x,y) = \int_0^{\pi} q(r,\theta)\Big|_{r = x\cos\theta + y\sin\theta} d\theta\,. \tag{2}$$

A. TO LEARN WINDOW FUNCTIONS

Eq. (1) shows that the projection $P(\omega,\theta)$ is multiplied by the ramp filter $filter_0(\omega) = |\omega|$ in the frequency domain in the original FBP. Note that this ramp filter is non-bounded and thus not realizable.

In practice, a window function $h(\omega)$ is usually added to the original ramp filter to enforce the values of $P(\omega,\theta)|\omega|$ outside a given frequency range to be zero, i.e., the original filter in Eq. (1) is replaced by the following combined filter:

$$filter\,(\omega) = h(\omega)\cdot|\omega|\,. \tag{3}$$

To get a better-reconstructed image, one should abide by the following principles: 1) the width of the main lobe should be narrow to get the steepest transition zone; and 2) the maximum side-lobe should be small, to improve the visual stationarity and increase the attenuation of the stopband [37]. The most common window function used in the original FBP is the rectangular window. The combined filter (*i.e.*, the ramp filter multiplied by a rectangular window function) is the so-called Ram-Lak filter, as shown in Fig. 1(a). However, the Ram-Lak filter may produce the Gibbs phenomenon [46], leading to ring artifacts in reconstructed images. To suppress these ring artifacts, several smooth windows were commonly used to replace the rectangular window function:

1. HAMMING WINDOW

$$h(\omega) = 0.54 + 0.46\cos\frac{\pi\omega}{2\Delta\omega K},$$

2. HANN WINDOW

$$h(\omega) = 0.5 + 0.5\cos\frac{\pi\omega}{2\Delta\omega K},$$

3. COSINE WINDOW

$$h(\omega) = \cos\frac{\pi\omega}{2\Delta\omega K},$$

4. SINE WINDOW

$$h(\omega) = \left(\sin\frac{\pi\omega}{2\Delta\omega K}\right)/\left(\frac{\pi\omega}{2\Delta\omega K}\right),$$

where $\omega = 0, \pm\Delta\omega, \pm 2\Delta\omega, \pm K\Delta\omega$ is the frequency value, K is an integer and $\Delta\omega$ is the frequency interval.

Fig. 1 displays several classical window functions, i.e. $h(\omega)$, used in FBP and their corresponding combined filters, i.e. $h(\omega) \cdot |\omega|$. We can see that the amplitude of the Ram-Lak filter increases linearly with frequency, which makes it susceptible to noise. Those smooth window functions make the trailing of the filter fade away, thus reducing its amplitude at high frequencies as shown in Figs. 1(b–e), which helps lower both noises and ringing artifacts. Although these smooth window functions are more robust to noises and ringing artifacts, they reduce the image resolution by introducing a blurring effect [47]. The quality of a reconstructed image depends on both the chosen filter and the cut-off frequency. A filter with a high cut-off frequency may enhance resolution and contrast, but cannot suppress noise effectively [37].

To achieve a balance between noise suppression and resolution enhancement, in this study, we propose a simple way to learn the filter directly from data using a specially designed pipeline as shown in Fig. 2. The sinogram on the left in Fig. 2 represents the projection. After performing a 1D fast Fourier transform (FFT), the sinogram is filtered with the learnable filter in the frequency domain, shown in the middle part in Fig. 2. At last, a 1D inverse Fourier transform is applied to the filtered data to recover the filtered projection p. The learnable filter in the frequency domain is directly defined as the optimizable vector instead of being modeled by neural networks to reduce the computational burden.

We used two strategies to learn the filter for FBP reconstruction:

- Strategy I: projections at all angles share the same filter. This strategy produces Filter I.
- Strategy II: projections at different angles use different filters. This strategy produces Filter II.

Filter I is consistent with the principle of traditional filter design, with parameters learned from data. Filter II can be regarded as a generalization of Filter I. It takes account of different angles in FBP. Filter I needs fewer parameters than Filter II, while Filter II keeps more diversity. The second column of Table 1 lists the number of optimizable parameters in the filter under the two strategies. In order to facilitate the whole end-to-end optimization, we initialized the learnable filter for both strategies from the “ram-lak” filter to speed up the convergence. We will test whether Filter II has a better performance than Filter I. Note that once Filter I and Filter II are trained, the computational complexity of FBP with the learned

filters is nearly the same as that with the original filter without bringing any additional computing time.

B. TO LEARN INTERPOLATION OPERATORS

Detectors used in CT include a series of discrete receivers, and the projection data is in discrete form and needs to use interpolation during the back-projection step. Linear interpolation is commonly used in FBP [48] as shown in Fig. 3(a) and can be expressed as:

$$p_{x_i, y_i, \theta} = (1 - z)p(a) + zp(a + 1), \tag{4}$$

where $p_{x_i, y_i, \theta}$ denotes the estimated intensity at the position (x_i, y_i) in the reconstruction image coming from the projection with angle θ, $a = \lfloor x_i \cos\theta + y_i \sin\theta \rfloor$ represents the corresponding detector position and $p(a)$ its projection value, and z is a weighted is a weighted parameter. This simple linear interpolation is sensitive to noise. Nearest interpolation, cubic spline interpolation, and piecewise cubic Hermite interpolation (PCHIP) [49] can be better options over linear interpolation. In this study, we design a learnable non-linear interpolation to replace the original linear interpolation used in FBP.

A linear combination of nearby projection points may not reflect one position's real value. We propose a non-linear interpolation for FBP reconstruction. We implement the nonlinear interpolation with a neural network for its strong linear and nonlinear expression ability. To this end, we first apply a non-linear transformation T to the projection p, i.e. $p' = T(p)$, where T is modeled by a neural network as shown in Fig. 3(b). Specifically, T consists of three residual blocks and a 1-dimension convolution layer. Each residual block sequentially comprises a 1-dimensional depth-wise convolution layer, 1-dimensional batch normalization (BN), and a parametric rectified linear unit (PRELU). A residual connection is applied from the input to the output within the residual block. By using all 1-dimension operations in T, we individually process each projection from different angles. The input to the network T has size $\mathrm{L} \times 360$, where L is the projection size and by 360 we mean projections from 360 different angles.

After obtaining the non-linearly transferred projection p', we then employ a linear combination to get $p_{x_i, y_i, \theta}$:

$$p_{x_i, y_i, \theta} = (1 - z)p'(a) + zp'(a + 1). \tag{5}$$

C. CNN-BASED POST-PROCESSING

To further improve the performance of our algorithm, we add an extra CNN module as a post-processing step for noise suppression in the image domain. There are many denoising, super-resolution networks that can be used directly in this step. In our study, a simple CNN module based on Lim et al's study [50] is used. It contains three residue blocks and three convolution blocks.

D. DeepFBP

Based on the learned filter and interpolation as well as the simple post-processing module, this new analytical FBP algorithm is termed as DeepFBP. The whole structure of DeepFBP is shown in Fig. 4. There are two versions of DeepFBP which use Filter I and Filter II respectively. We name them as DeepFBP I and DeepFBP II.

The numbers of parameters of each component in DeepFBP are listed in Table 1. The proposed method is lightweight, especially for the Filter I version. Our method are much lighter than some commonly used denoising networks in CT such as the Cascaded-CNN [19] which has 1.1 million parameters. Our method has less than 0.61 million parameters.

During the training phase, DeepFBP sequentially transfers the initial projection across the learnable filter, non-linear interpolation, and post-processing network, to generate the final CT image. The L2 loss between the reconstructed CT image and the normal-dose CT image is then computed, and subsequently, the gradient of the loss back-propagates through all learnable modules to achieve gradient-based optimization. The detailed training settings are given in Section III–E.

III. DATASETS AND EVALUATIONS

In this section, we introduce datasets used in this study and evaluation metrics for algorithm evaluation. We use a clinical patient dataset from Mayo Clinics for “the 2016 NIH-AAPM-Mayo Clinic Low Dose CT Grand Challenge” [18](hereinafter referred to as “AAPM dataset”). It includes twelve patients’ normal and low-dose scans. Three kinds of projections are tested: *low-dose projections*, *noisy normal-dose projections,* and *sparse-view low-dose projections*. In each case, we chose ten patients as the training dataset (2039 2D pairs), one patient as the validation data (128 2D pairs), and the last one as the test data (211 2D pairs).

A. LOW-DOSE PROJECTIONS

Low-dose scans in the AAPM dataset are projected into 360 angles with an angle interval of 0.5° to generate *low-dose projections*. Reconstruction algorithms are applied to these *low-dose projections* to obtain *low-dose reconstructions*.

B. NOISY NORMAL-DOSE PROJECTION

Normal-dose scans are used to generate normal-dose projections, which are added noise to obtain *noisy normal-dose projections*. According to previous studies [51], [52], [53], [54], [55], CT noise can be assumed to be Poisson-distributed quantum noise plus Gaussian-distributed electronic noise, which is:

$$n_i = Poisson\left(I_0 e^{-p^i}\right) + Gaussian\left(0, \sigma_e^2\right),$$

where n_i is noise over the i-th projection p^i, $Poisson(\cdot)$ and $Gaussian(0, \cdot)$ denote the Poisson distribution and the zeromean Gaussian distribution respectively, $I_0 e^{-p^i}$ is the noisy transmission datum according to the Lambert-Beer law, I_0 denotes the incident X-ray

intensity, and σ_e^2 is the background electronic noise variance. According to several clinical studies [55], [56], [57], [58], [59], I_0 is set as 1.0×10^5, and the electronic noise variance σ_e^2 is set as 10.

C. SPARSE-VIEW LOW-DOSE PROJECTIONS

By cutting down the projection angle from 360 to 90, we used low-dose scans to generate *sparse-view low-dose projections*. Reconstruction algorithms are applied to these projections to obtain *sparse-view low-dose reconstructions*.

D. EVALUATION CRITERIA

Peak signal-to-noise ratio (PSNR) and structural similarity (SSIM) are adopted to evaluate the reconstructed images. PSNR is defined as:

$$PSNR = 10 \cdot log_{10} \frac{\mu_{max}^2}{MSE},$$

where MSE is the mean-squared error between the reconstructed image and the reference image and μ_{max} is the maximum possible value of the image. Higher PSNR means less error between the reconstructed image and the reference image [14]. SSIM is defined as:

$$SSIM\ (a, b) = \frac{(2\mu_a\mu_b + C_1)(2\sigma_{ab} + C_2)}{(\mu_a^2 + \mu_b^2 + C_1)(\sigma_a^2 + \sigma_b^2 + C_2)},$$

where a and b are two local windows of size 8×8 pixels in two images. The two windows have the same position, and μ_a and σ_a, μ_b and σ_b are their mean and standard deviation, respectively, σ_{ab} is the covariance between the two windows, and C_1 and C_2 are two constants to avoid instability. In this study, C_1 and C_2 are chosen as $C_1 = (0.01\ \mu_{max})^2$ and $C_2 = (0.03\ \mu_{max})^2$. SSIM is used to measure the similarity in the structure between the two windows where a higher value means higher similarity. As the two windows move pixel-by-pixel over the reconstructed image and the reference image, we obtain an SSIM map. In practice, we use a single Mean-SSIM (MSSIM) value to evaluate the overall image quality by simply averaging the SSIM values [14].

E. TRAINING SETTINGS

For all experiments, we use AdamW as the optimizer with default network initialization. The loss function is the L_2 loss. All experiments are done on an RTX 2080Ti GPU. In Section II, we have proposed two DeepFBP versions for CT reconstruction (DeepFBP I and DeepFBP II). Both have three new learnable components, namely, the learned filter (window function), the learned interpolation, and the post-processing module.

The training of DeepFBP is divided into three phases. First, we pre-train the network with learnable filters and interpolation only. The training epoch is 200, the learning rate is $1e^{-3}$. The second phase uses pre-trained parameters from the first phase, and only updates parameters of the post-processing part. The training epoch is 100 and the learning rate is

$1e^{-3}$. In the third phase, all the parameters of the three learnable parts are updated together. The training epoch is 100 and the learning rate is $1e^{-4}$. We use a batch size of 8 for all the experiments.

IV. EXPERIMENT

A. COMPARISON METHODS

We compare the proposed methods, *i.e.*, DeepFBP I and DeepFBP II, with four other methods, which are FBP, TV-based statistical iterative algorithm, FBPConvNet [60], and RED-CNN [18]. FBP is the most classic algorithm for CT reconstruction. We chose the Ram-Lak filter and linear interpolation for FBP. The TV-based iterative algorithm is commonly used for CT reconstruction and shows a good ability to preserve edges and suppress noise. It is often used as a baseline [26], [60]. Both FBPConvNet and RED-CNN are post-processing algorithms, providing state-of-the-art performance for CT reconstruction. They utilize deep learning networks to enhance the rough images reconstructed by FBP. In our experiments, we train FBPConvNet and RED-CNN using the pairs of rough images and their normal-dose references.

B. LOW-DOSE RECONSTRUCTION

In this part, we compare DeepFBP with others over the *low-dose projections*. The performance on the validation set and test set is listed in Table 2.

As shown in Table 2, two DeepFBP algorithms achieve the best performance among all methods. DeepFBP II improves the PSNR by nearly 3dB over the classical FBP and nearly 2dB over FBPConvNet. Both DeepFBP I and DeepFBP II exceed RED-CNN.

To visualize reconstruction quality, we display one reconstructed slice from the test set in Fig. 5. The blue rectangle is the region of interest (ROI) and is enlarged at the left bottom of each subfigure. Both DeepFBP I and DeepFBP II have better reconstruction visual quality than FBP, the TV algorithm, FBPConvNet [60], and RED-CNN [18]. Particularly, both DeepFBP algorithms suppress noise and preserve edges very well. They are also good at removing the staircase effect that typically presents in the TV algorithm. Both DeepFBP algorithms obtain CT images with less noise than FBPConvNet and RED-CNN.

C. NOISY NORMAL-DOSE RECONSTRUCTION

In this part, we apply all methods over *noisy normal-dose projections*. The results are listed in Table 3.

As shown in Table 3, the traditional FBP algorithm and the TV-based iteration algorithm show their limitations in processing the noisy projection. Among deep-learning-based methods, DeepFBP II achieves the best performance.

Fig. 6 shows one slice of the reconstruction images. As one can see, the results of FBP and the TV-based method are of quite low quality. Details are lost in Fig. 6(a) and Fig. 6(b). By comparison, both FBPConvNet and RED-CNN are able to improve reconstruction quality.

Two DeepFBP algorithms, especially DeepFBP II, show the best visual performance and suppress noise the most successfully.

D. SPARSE-VIEW LOW-DOSE RECONSTRUCTION

In this part, we apply DeepFBP and other methods over *sparse-view low-dose projections*. The performance on the validation set and the test set is listed in Table 4.

These results are even more impressive. Our methods improve the PSNR by about 7dB over FBP, 5dB over the TV method, and 1dB over FBPConvNet and RED-CNN. These results indicate that when there is a large loss of information in projection, the two DeepFBP algorithms became more competitive compared with others. This mainly benefits from both the learned filter and the learned interpolation.

To visualize the image quality from *sparse-view low-dose reconstruction*, we display a reconstruction slice in the test set in Fig. 7. As shown in Fig. 7 (a, b), FBP and TV have excessive artifacts. Both FBPConvNet and RED-CNN alleviate these artifacts (Fig. 7 (c, d)). The proposed DeepFBP I (Fig. 7 (e)) and DeepFBP II (Fig. 7 (f)) have much fewer artifacts compared with all other methods.

E. LEARNED FILTERS IN DIFFERENT CASES

In this part, we show learned filters. Filters in DeepFBP I are the same at all angles while those in DeeFBP II are different at each angle. From Fig. 8 to Fig. 10, we plot Filter I, the mean of Filter II, Filter II at the angle 0° and 90°, learned in the above experiments.

In general, all learned filters keep symmetry. Filters learned in each case do not look the same and have their unique characteristics. As shown in Fig. 8, in the *low-dose projection* case, Filter I and Filter II are both similar to the Ram-Lak filter. Filter II differs slightly at different angles but looks similar. In the *noisy normal-dose projection* case, as shown in Fig. 9, Filter I and Filter II do not look the same. Filter I has multi-peaks while the mean of Filter II seems like the Ram-Lak filter, and Filter II is still like the Ram-Lak filter at different angles but with slight perturbations. In the sparse-view reconstruction, Filter I and Filter II differ a lot both in shape and data range. Filter II exhibits significant difference at 0° and 90° in the *sparse-view low-dose reconstruction*.

F. COMPUTATION EFFICIENCY STUDY

In CT reconstruction, speed is also an important factor to consider. Analytical algorithms are more widely used in clinical scanners than statistical iterative algorithms. We analyzed the computational time of each component in the proposed DeepFBP algorithms, compared with FBP.

From Table 5, we can find that the proposed methods are a little bit slower than the original FBP, but the gap is very small especially when a GPU is used. Additionally, compared to the TV-based iterative algorithm, the proposed methods are two orders of magnitude faster.

V. DISCUSSION

In this study, we derive a novel analytical method for CT reconstruction named DeepFBP. To construct DeepFBP, we replace standard components in FBP with simple and small neural network modules. These modules include a learnable frequency-filter module, a learnable non-linear interpolation module, and a simple post-processing module. Compared with those post-processing deep learning reconstruction methods such as FBPConvNet [60] and RED-CNN [18], DeepFBP can make better use of projection information and is highly interpretable. We believe these are important advantages for medical imaging. Experiments on three kinds of projections demonstrated the high performance of the proposed DeepFBP methods both quantitatively and visually.

One of our motivations is to improve the performance of the analytical filtered back-projection for low-dose CT reconstruction. FBP is much faster than iterative reconstructions but with worse reconstruction quality. A natural question to ask is: could the analytical reconstruction achieve comparable performance as iterative reconstructions while still maintaining high computational efficiency? Previous studies [29], [30], [31] have shown that modifying the filter in FBP could improve its performance. However, the performance of these FBP variants is still not as good as iterative reconstructions. In this study, we propose DeepFBP to optimize both the filter and the nonlinear interpolation with simple neural networks for the classical FBP. The proposed DeepFBP algorithms can achieve better performance than the TV-based iterative reconstruction algorithm and two state-of-the-art post-processing deep learning reconstruction methods (FBPConvNet [60] and RED-CNN [18]) while keeping the speed advantage of FBP.

One question is which part of FBP can be modified without sacrificing its computational speed. Because of the important role of the filtering step in FBP, we modify it to a data-driven form that can be learned from the training dataset. This modification does not increase the computational burden but can greatly improve the performance while having a good ability of interpretation. Taking the ray divergence into consideration, we also propose a learnable data-dependent non-linear interpolation method, which is more robust to the noise by using the information of adjacent detector bins.

We compare our DeepFBP methods with two state-of-the-art post-processing deep learning methods for CT reconstruction, namely, FBPConvNet [60] and RED-CNN [18]. RED-CNN is a very deep fully convolutional encoding-decoding framework for image restoration such as denoising and super-resolution [17]. FBPConvNet, on the other hand, can be considered as a refinement of the multi-resolution U-net structure [61] with a skip connection between input and output [62]. Note that the proposed DeepFBP used much simpler networks than those in RED-CNN and FBPConvNet. Surprisingly, the DeepFBP algorithm did easily outperform both FBPConvNet and RED-CNN in all cases in our experiments. A possible reason might be DeepFBP takes full usage of information of the reconstruction process, whereas these two post-processing methods treat reconstruction as an image restoration problem and totally ignore the physical behaviors and properties in the reconstruction. Our study indicates that taking into account the reconstruction process is important for designing a high-quality reconstruction algorithm.

Although the proposed new analytical reconstruction method showed good performance and short computational time, there are still several aspects that can be further improved. For example, the filters need to be retrained for different noise situations in our current DeepFBP. It can be re-designed to be self-adaptive to different noise levels.

VI. CONCLUSION

In this work, we propose a new analytical method named DeepFBP for CT reconstruction. In this method, the filter and the interpolation method in the projection domain are learned from data using neuron networks. Experiments on the AAPM dataset demonstrate that DeepFBP not only achieved better performance than the TV-based iterative reconstruction method and two state-of-the-art post-processing deep learning methods but also kept the computational advantage of FBP.

ACKNOWLEDGMENT

The authors would like to thank Dr. Cynthia H. McCollough in Mayo Clinics for providing “the 2016 NIH-AAPM-Mayo Clinic Low Dose CT Grand Challenge” dataset.

This work was supported in part by the National Natural Science Foundation of China (NNSFC) under Grant 62071197. The work of Jing Wang was supported in part by the Cancer Prevention and Research Institute of Texas under Grant RP160661, and in part by the National Institute of Biomedical Imaging and Bioengineering under Grant R01 EB027898.

Biographies

XI TAN received the B.S. degree in computer science from Wuhan University, Wuhan, China, in 1989, and the M.S. degree in computer science from Central South University, Changsha, China, in 2007. From 1989 to 2003, he was a Senior Engineer in computer architecture and signal measurement with Zhuzhou Cemented Carbide Group Company Ltd. From 2004 to 2005, he was a Visiting Professor with Tokyo Denki University, Japan. Since 2007, he has been a Professor with the College of Electrical and Information Engineering, Hunan University of Technology, Zhuzhou, China. His research interests include embedded systems, signal measurement, pattern recognition, computer vision, and their applications in industry.

XUAN LIU received the B.E. degree in automation from the Huazhong University of Science and Technology, in 2019, where he is currently pursuing the Ph.D. degree with

the School of Artificial Intelligence and Automation. He is an Intern with the Institute of Biomedical and Health Engineering, Shenzhen Institutes of Advanced Technology, Chinese Academy of Sciences. His research interests include medical image computing and image inverse problems, particularly focus on low-dose CT reconstruction.

KAI XIANG, photograph and biography not available at the time of publication.

JING WANG, photograph and biography not available at the time of publication.

SHAN TAN, photograph and biography not available at the time of publication.

REFERENCES

[1]. De Gonzalez AB, Mahesh M, and Kim KP, "Projected cancer risks from computed tomographic scans performed in the United States in 2007," JAMA Internal Med., vol. 169, no. 22, pp. 2071–2077, 2009.

[2]. Kalra MK, Maher MM, Toth TL, Hamberg LM, Blake MA, Shepard J-A, and Saini S, "Strategies for CT radiation dose optimization," Radiology, vol. 230, no. 3, pp. 619–628, Mar. 2004. [PubMed: 14739312]

[3]. Ren Z, Liu G, and Huang Z, "Study on an improved filtered back-projection image reconstruction algorithm combined with wavelet denoising," Proc. SPIE, vol. 8907, pp. 251–259, Sep. 2013.

[4]. Nielsen T, Hitziger S, Grass M, and Iske A, "Filter calculation for X-ray tomosynthesis reconstruction," Phys. Med. Biol, vol. 57, no. 12, pp. 3915–3930, Jun. 2012. [PubMed: 22643063]

[5]. Qu H-Y, Xu F, Hu X-F, Wang L-B, Zhao J, and Zhang Z, "A novel denoising method based on radon transform and filtered back-projection reconstruction algorithm," Opt. Lasers Eng, vol. 50, no. 4, pp. 593–598, Apr. 2012.

[6]. Pelt DM and Batenburg KJ, "Improving filtered backprojection reconstruction by data-dependent filtering," IEEE Trans. Image Process, vol. 23, no. 11, pp. 4750–4762, Nov. 2014. [PubMed: 25069117]

[7]. Mu C and Park C, "Optimal filtered backprojection for fast and accurate tomography reconstruction," 2016, arXiv:1608.01686.

[8]. Gordon R, Bender R, and Herman GT, "Algebraic reconstruction techniques (ART) for three-dimensional electron microscopy and X-ray photography," J. Theor. Biol, vol. 29, no. 3, pp. 471–481, Dec. 1970. [PubMed: 5492997]

[9]. Jiang M and Wang G, "Convergence studies on iterative algorithms for image reconstruction," IEEE Trans. Med. Imag, vol. 22, no. 5, pp. 569–579, May 2003.

[10]. Andersen A, "Simultaneous algebraic reconstruction technique (SART): A superior implementation of the ART algorithm," Ultrason. Imag, vol. 6, no. 1, pp. 81–94, Jan. 1984.

[11]. Rudin LI, Osher S, and Fatemi E, "Nonlinear total variation based noise removal algorithms," Phys. D, Nonlinear Phenomena, vol. 60, nos. 1–4, pp. 259–268, Nov. 1992.

[12]. Zhang Y, Tehrani JN, and Wang J, "A biomechanical modeling guided CBCT estimation technique," IEEE Trans. Med. Imag, vol. 36, no. 2, pp. 641–652, Feb. 2017.

[13]. Bredies K, Kunisch K, and Pock T, "Total generalized variation," SIAM J. Imag. Sci, vol. 3, no. 3, pp. 492–526, 2010.

[14]. Sun T, Sun N, Wang J, and Tan S, "Iterative CBCT reconstruction using Hessian penalty," Phys. Med. Biol, vol. 60, no. 5, pp. 1965–1987, Mar. 2015. [PubMed: 25674998]

[15]. Shi Q, Sun N, Sun T, Wang J, and Tan S, "Structure-adaptive CBCT reconstruction using weighted total variation and Hessian penalties," Biomed. Opt. Exp, vol. 7, no. 9, p. 3299, 2016.

[16]. Liu L, Li X, Xiang K, Wang J, and Tan S, "Low-dose CBCT reconstruction using Hessian schatten penalties," IEEE Trans. Med. Imag, vol. 36, no. 12, pp. 2588–2599, Dec. 2017.

[17]. Mao X, Shen C, and Yang Y-B, “Image restoration using very deep convolutional encoder–decoder networks with symmetric skip connections,” in Proc. Adv. Neural Inf. Process. Syst, 2016, pp. 2802–2810.

[18]. Chen H, Zhang Y, Kalra MK, Lin F, Chen Y, Liao P, Zhou J, and Wang G, “Low-dose CT with a residual encoder–decoder convolutional neural network,” IEEE Trans. Med. Imag, vol. 36, no. 12, pp. 2524–2535, Dec. 2017.

[19]. Wu D, Kim K, El Fakhri G, and Li Q, “A cascaded convolutional neural network for X-ray low-dose CT image denoising,” 2017, arXiv:1705.04267.

[20]. Zhang K, Zuo W, Chen Y, Meng D, and Zhang L, “Beyond a Gaussian denoiser: Residual learning of deep CNN for image denoising,” IEEE Trans. Image Process, vol. 26, no. 7, pp. 3142–3155, Jul. 2017. [PubMed: 28166495]

[21]. Johnson J, Alahi A, and Fei-Fei L, “Perceptual losses for real-time style transfer and super-resolution,” in Proc. Eur. Conf. Comput. Vis Cham, Switzerland: Springer, 2016, pp. 694–711.

[22]. Yang Q, Yan P, Zhang Y, Yu H, Shi Y, Mou X, Kalra MK, Zhang Y, Sun L, and Wang G, “Low-dose CT image denoising using a generative adversarial network with Wasserstein distance and perceptual loss,” IEEE Trans. Med. Imag, vol. 37, no. 6, pp. 1348–1357, Jun. 2018.

[23]. Shan H, Zhang Y, Yang Q, Kruger U, Kalra MK, Sun L, Cong W, and Wang G, “3-D convolutional encoder–decoder network for low-dose CT via transfer learning from a 2-D trained network,” IEEE Trans. Med. Imag, vol. 37, no. 6, pp. 1522–1534, Jun. 2018.

[24]. Wolterink JM, Leiner T, Viergever MA, and Išgum I, “Generative adversarial networks for noise reduction in low-dose CT,” IEEE Trans. Med. Imag, vol. 36, no. 12, pp. 2536–2545, Dec. 2017.

[25]. Goodfellow I, Pouget-Abadie J, Mirza M, Xu B, Warde-Farley D, Ozair S, Courville A, and Bengio Y, “Generative adversarial nets,” in Proc. Adv. Neural Inf. Process. Syst, 2014, pp. 2672–2680.

[26]. Adler J and Öktem O, “Learned primal-dual reconstruction,” IEEE Trans. Med. Imag, vol. 37, no. 6, pp. 1322–1332, Jun. 2018.

[27]. Wu D, Kim K, El Fakhri G, and Li Q, “Iterative low-dose CT reconstruction with priors trained by artificial neural network,” IEEE Trans. Med. Imag, vol. 36, no. 12, pp. 2479–2486, Dec. 2017.

[28]. Chen B, Xiang K, Gong Z, Wang J, and Tan S, “Statistical iterative CBCT reconstruction based on neural network,” IEEE Trans. Med. Imag, vol. 37, no. 6, pp. 1511–1521, Jun. 2018.

[29]. Syben C, Stimpel B, Breininger K, Würfl T, Fahrig R, Dörfler A, and Maier A, “Precision learning: Reconstruction filter kernel discretization,” 2017, arXiv:1710.06287.

[30]. Würfl T, Hoffmann M, Christlein V, Breininger K, Huang Y, Unberath M, and Maier AK, “Deep learning computed tomography: Learning projection-domain weights from image domain in limited angle problems,” IEEE Trans. Med. Imag, vol. 37, no. 6, pp. 1454–1463, Jun. 2018.

[31]. He J, Wang Y, and Ma J, “Radon inversion via deep learning,” IEEE Trans. Med. Imag, vol. 39, no. 6, pp. 2076–2087, Jun. 2020.

[32]. Ramachandran GN and Lakshminarayanan AV, “Three-dimensional reconstruction from radiographs and electron micrographs: Application of convolutions instead of Fourier transforms,” Proc. Nat. Acad. Sci. USA, vol. 68, no. 9, pp. 2236–2240, Sep. 1971. [PubMed: 5289381]

[33]. Kaiser J and Hamming R, “Sharpening the response of a symmetric nonrecursive filter by multiple use of the same filter,” IEEE Trans. Acoust., Speech, Signal Process, vol. ASSP-25, no. 5, pp. 415–422, Oct. 1977.

[34]. Gonzales RC and Woods RE, Digital Image Processing. Upper Saddle River, NJ, USA: Prentice-Hall, 2002.

[35]. Rife DC and Vincent GA, “Use of the discrete Fourier transform in the measurement of frequencies and levels of tones,” Bell Syst. Tech. J, vol. 49, no. 2, pp. 197–228, Feb. 1970.

[36]. King MA, Schwinger RB, Doherty PW, and Penney BC, “Two-dimensional filtering of SPECT images using the Metz and Wiener filters,” J. Nucl. Med, vol. 25, no. 11, pp. 1234–1240, 1984. [PubMed: 6333497]

[37]. Yu S, “Application of Parzen window in filter back projection algorithm,” IOP Conf. Ser., Mater. Sci. Eng, vol. 392, no. 6, 2018, Art. no. 062183.

[38]. Farquhar TH, Chatziioannou A, Chinn G, Dahlbom M, and Hoffman EJ, "An investigation of filter choice for filtered backprojection reconstruction in PET," IEEE Trans. Nucl. Sci, vol. 45, no. 3, pp. 1133–1137, Jun. 1998.

[39]. Zeng GL and Zamyatin A, "A filtered backprojection algorithm with ray-by-ray noise weighting," Med. Phys., vol. 40, no. 3, Mar. 2013, Art. no. 031113.

[40]. Zeng GL, "A filtered backprojection algorithm with characteristics of the iterative Landweber algorithm," Med. Phys, vol. 39, no. 2, pp. 603–607, Jan. 2012. [PubMed: 22320769]

[41]. Brooks RA, Weiss GH, and Talbert AJ, "A new approach to interpolation in computed tomography," J. Comput. Assist. Tomogr, vol. 2, no. 5, pp. 577–585, Nov. 1978. [PubMed: 711944]

[42]. Wang J, Lu H, Li T, and Liang Z, "An alternative solution to the nonuniform noise propagation problem in fan-beam FBP image reconstruction," Med. Phys, vol. 32, no. 11, pp. 3389–3394, Nov. 2005. [PubMed: 16372414]

[43]. Horbelt S, Liebling M, and Unser MA, "Filter design for filtered backprojection guided by the interpolation model," Proc. SPIE, vol. 4684, pp. 806–813, Mar. 2002.

[44]. Kalender WA, Fuchs T, Krause J, Klingenbeck K, Flohr T, and Schaller S, "Spiral interpolation algorithm for multislice spiral CT. I. Theory," IEEE Trans. Med. Imag, vol. 19, no. 9, pp. 822–834, Feb. 2000.

[45]. McCann MT and Unser M, "High-quality parallel-ray X-ray CT back projection using optimized interpolation," IEEE Trans. Image Process, vol. 26, no. 10, pp. 4639–4647, Oct. 2017. [PubMed: 28541206]

[46]. Gottlieb D and Shu C-W, "On the Gibbs phenomenon and its resolution," SIAM Rev, vol. 39, no. 4, pp. 644–668, Jan. 1997.

[47]. Zeng GL, "Revisit of the ramp filter," in Proc. IEEE Nucl. Sci. Symp. Med. Imag. Conf. (NSS/MIC), Nov. 2014, pp. 1–6.

[48]. Kak AC, Slaney M, and Wang G, "Principles of computerized tomographic imaging," Med. Phys, vol. 29, no. 1, p. 107, Jan. 2002.

[49]. Davis PJ, Interpolation and Approximation. North Chelmsford, MA, USA: Courier Corp., 1975.

[50]. Lim B, Son S, Kim H, Nah S, and Lee KM, "Enhanced deep residual networks for single image super-resolution," in Proc. IEEE Conf. Comput. Vis. Pattern Recognit. Workshops (CVPRW), Jul. 2017, pp. 1132–1140.

[51]. Wang J and Gu X, "High-quality four-dimensional cone-beam CT by deforming prior images," Phys. Med. Biol, vol. 58, no. 2, pp. 231–246, Jan. 2013. [PubMed: 23257113]

[52]. Liu Y, Ma J, Fan Y, and Liang Z, "Adaptive-weighted total variation minimization for sparse data toward low-dose X-ray computed tomography image reconstruction," Phys. Med. Biol, vol. 57, no. 23, pp. 7923–7956, Dec. 2012. [PubMed: 23154621]

[53]. La Riviere PJ, Bian J, and Vargas PA, "Penalized-likelihood sinogram restoration for computed tomography," IEEE Trans. Med. Imag, vol. 25, no. 8, pp. 1022–1036, Aug. 2006.

[54]. Xu J and Tsui BMW, "Electronic noise modeling in statistical iterative reconstruction," IEEE Trans. Image Process, vol. 18, no. 6, pp. 1228–1238, Jun. 2009. [PubMed: 19398410]

[55]. Ma J, Liang Z, Fan Y, Liu Y, Huang J, Chen W, and Lu H, "Variance analysis of X-ray CT sinograms in the presence of electronic noise background," Med. Phys, vol. 39, no. 7, pp. 4051–4065, Jun. 2012. [PubMed: 22830738]

[56]. Wang J, Li T, Lu H, and Liang Z, "Penalized weighted least-squares approach to sinogram noise reduction and image reconstruction for low-dose X-ray computed tomography," IEEE Trans. Med. Imag, vol. 25, no. 10, pp. 1272–1283, Oct. 2006.

[57]. Defrise M, Vanhove C, and Liu X, "An algorithm for total variation regularization in high-dimensional linear problems," Inverse Problems, vol. 27, no. 6, Jun. 2011, Art. no. 065002.

[58]. Lasio GM, Whiting BR, and Williamson JF, "Statistical reconstruction for X-ray computed tomography using energy-integrating detectors," Phys. Med. Biol, vol. 52, no. 8, pp. 2247–2266, Apr. 2007. [PubMed: 17404467]

[59]. O'Sullivan JA and Benac J, "Alternating minimization algorithms for transmission tomography," IEEE Trans. Med. Imag, vol. 26, no. 3, pp. 283–297, Mar. 2007.

[60]. Jin KH, McCann MT, Froustey E, and Unser M, “Deep convolutional neural network for inverse problems in imaging,” IEEE Trans. Image Process, vol. 26, no. 9, pp. 4509–4522, Sep. 2017. [PubMed: 28641250]

[61]. Ronneberger O, Fischer P, and Brox T, “U-Net: Convolutional networks for biomedical image segmentation,” in Proc. Int. Conf. Med. Image Comput. Comput.-Assist. Intervent., 2015, pp. 1–12.

[62]. Kim J, Lee JK, and Lee KM, “Accurate image super-resolution using very deep convolutional networks,” in Proc. IEEE Conf. Comput. Vis. Pattern Recognit. (CVPR), Jun. 2016, pp. 1646–1654.

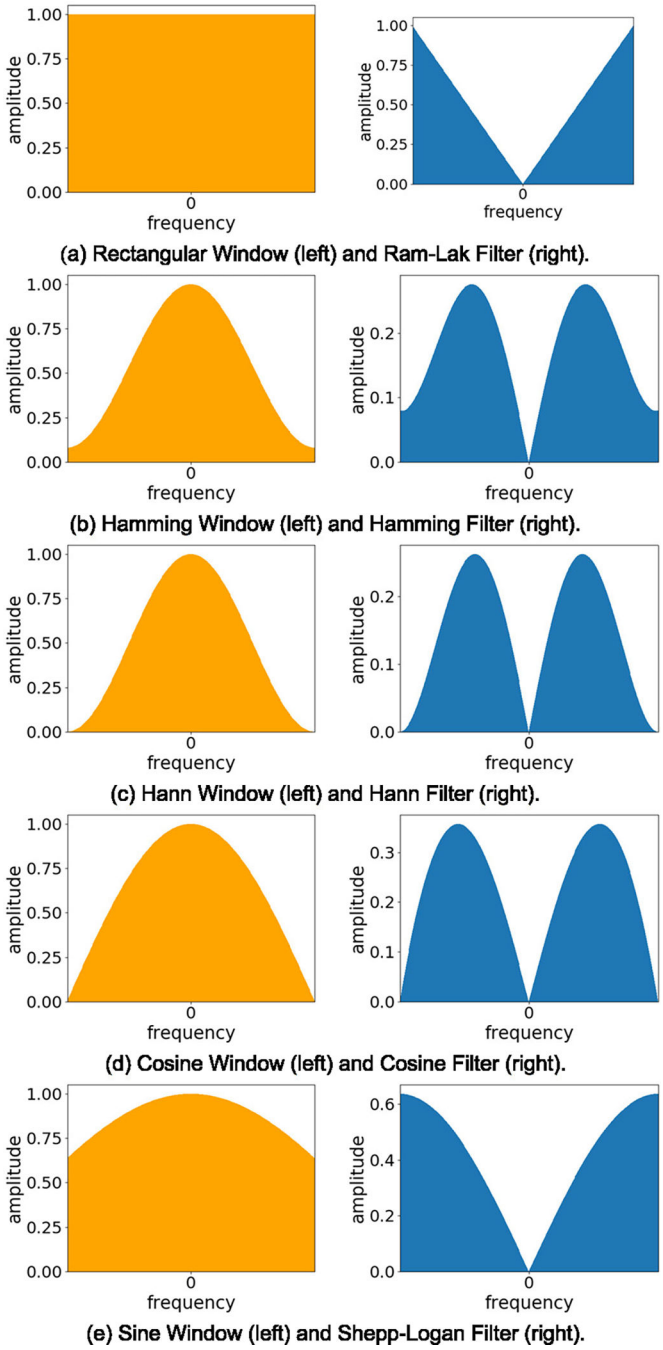

FIGURE 1. Window functions and their corresponding filters commonly used in FBP.

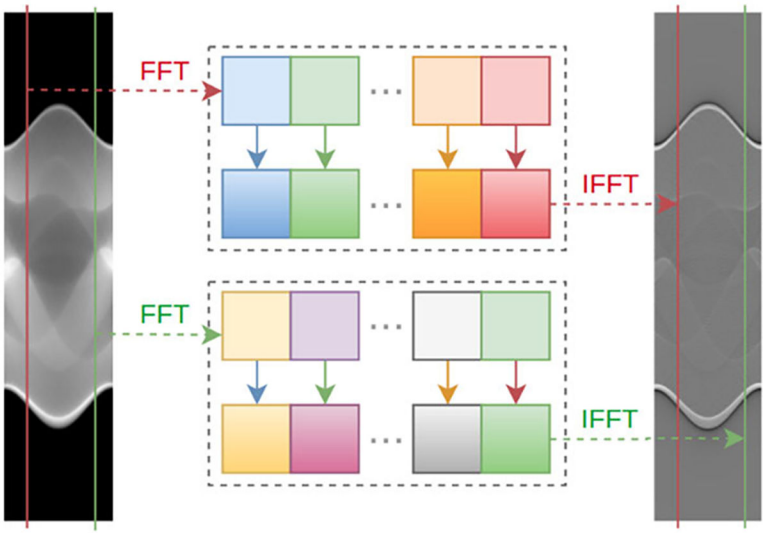

FIGURE 2. Filtering operation with the learnable filter.

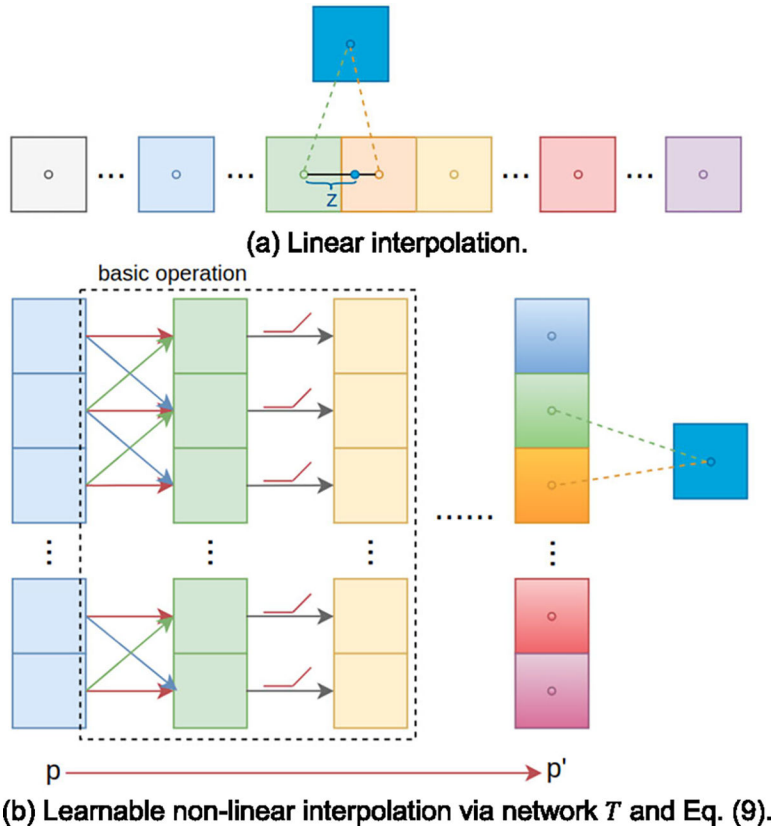

FIGURE 3. Interpolation operation in reconstruction.

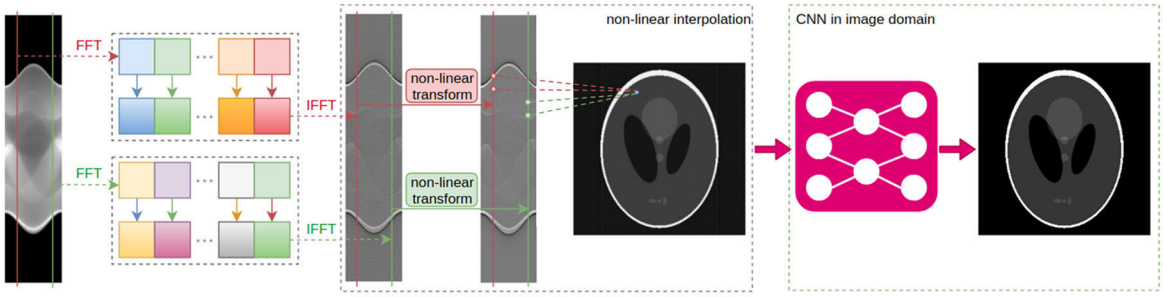

FIGURE 4. Structure of the proposed DeepFBP, which consists of the learnable filter, non-linear interpolation, and post-processing network. During the training phase, we supervise these optimizable modules through L2 loss and normal-dose CT images. During the test phase, DeepFBP directly restores the high-quality CT image from the degraded projection.

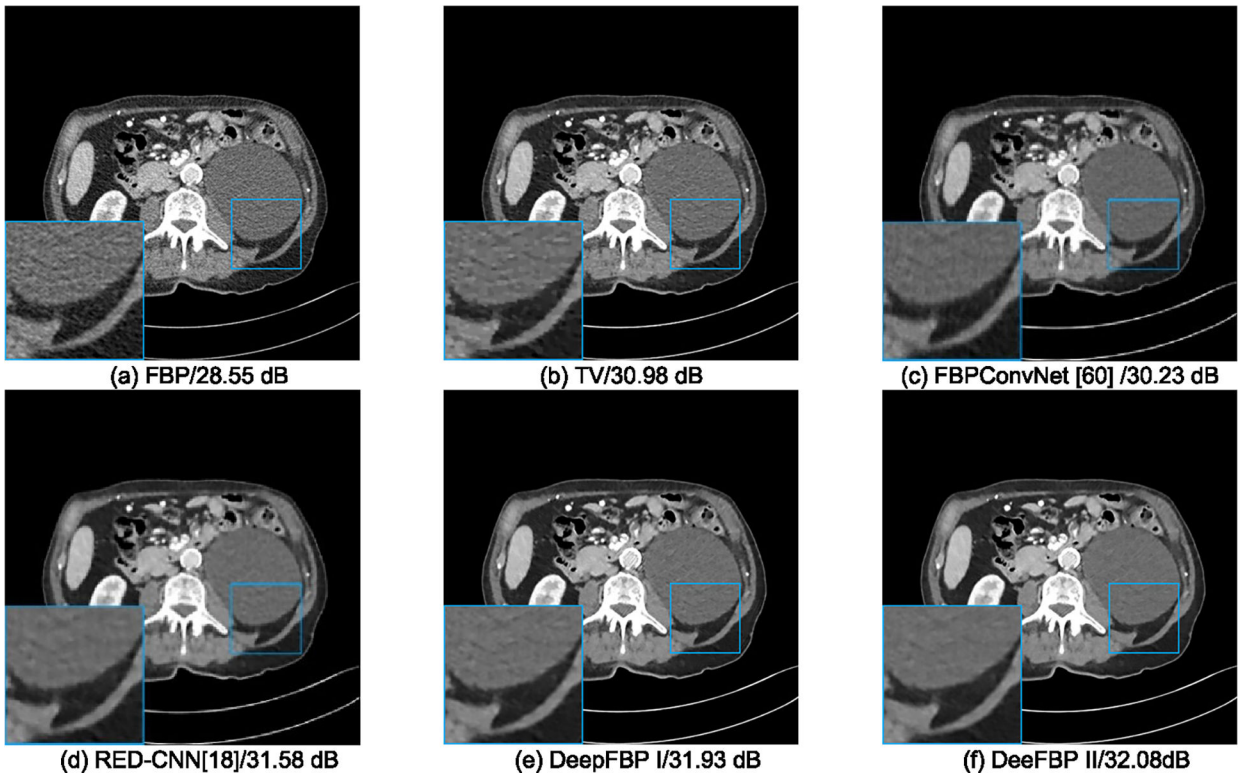

FIGURE 5. Results of a low-dose reconstruction. The display window is [−160, 240] HU.

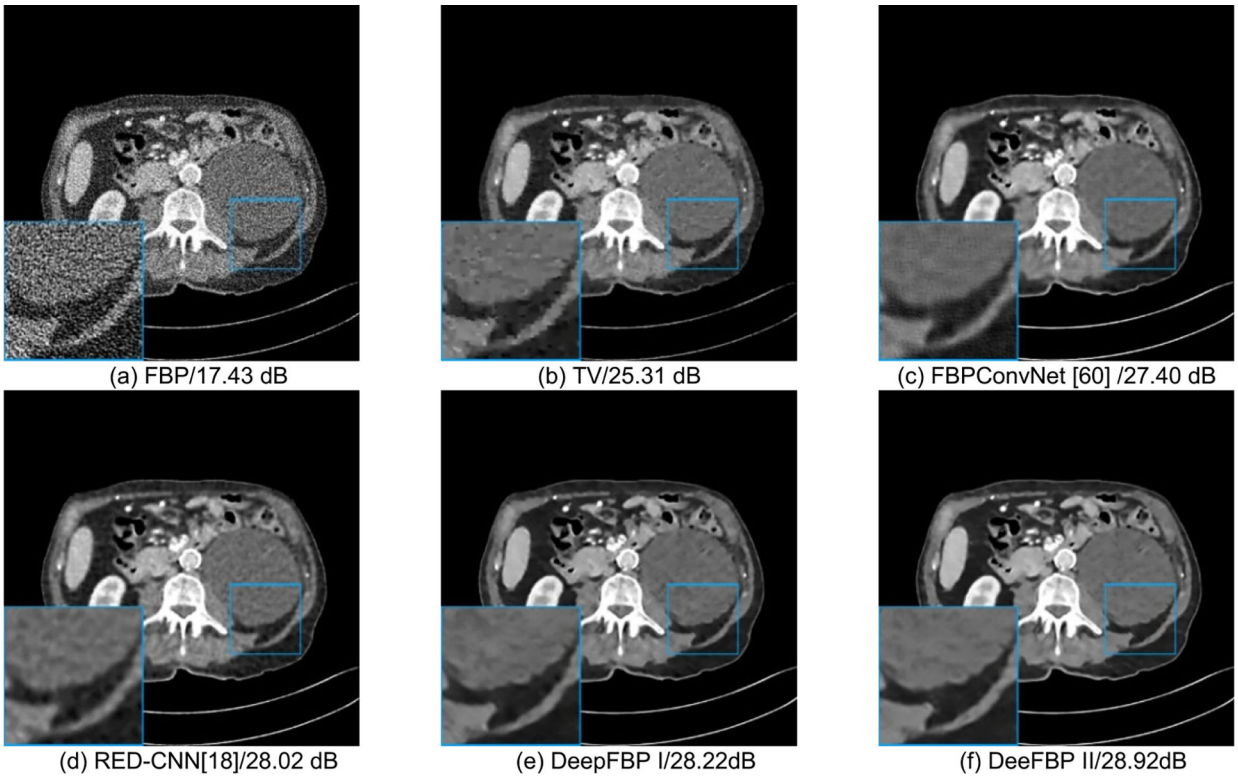

FIGURE 6. Results of a *noisy normal-dose reconstruction*. The display window is [−160, 240] HU.

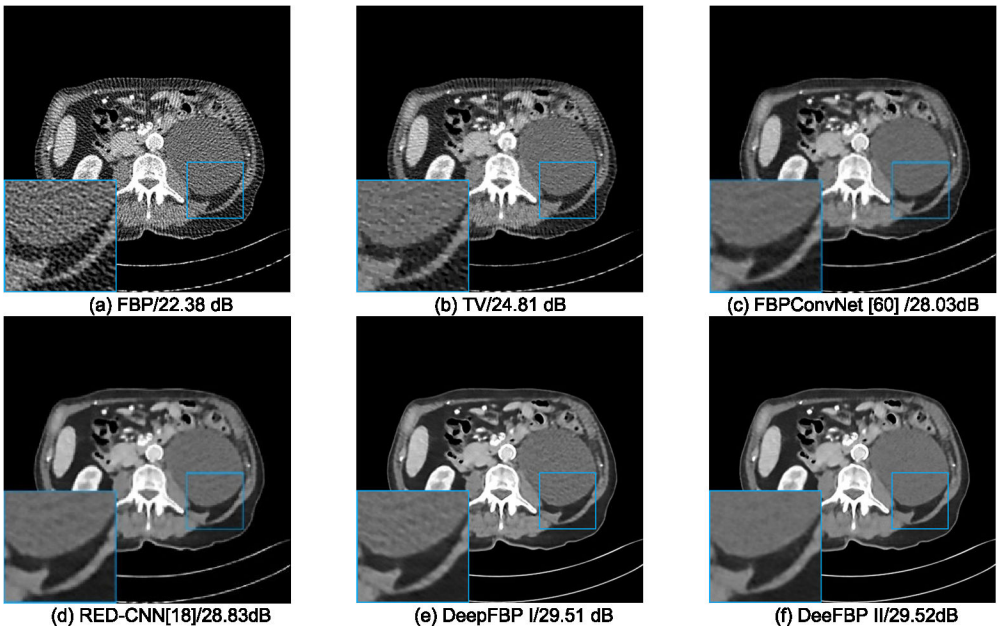

FIGURE 7. Results of a *sparse-view low-dose reconstruction* (90 angles). The display window is [−160, 240] HU.

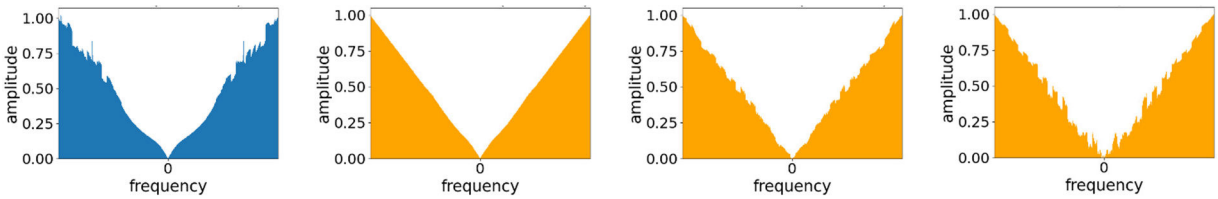

FIGURE 8. Filters learned in *low-dose reconstruction*.

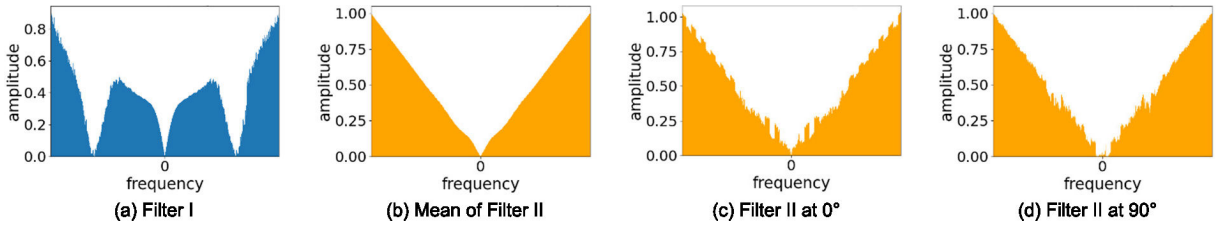

FIGURE 9. Filters learned in *noisy normal-dose reconstruction.*

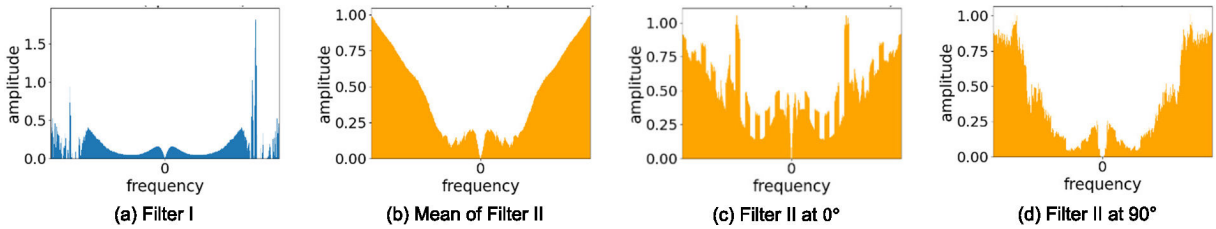

FIGURE 10. Filters learned in *sparse-view low-dose reconstruction*.

TABLE 1.

Number of parameters in DeepFBP for images of size 512 × 512.

	Filter	Interp	Post	Total
DeepFBP I	1,024	12,603	223,606	237,233
DeepFBP II	368,640	12,603	223,606	604,849

Note: Interp means the leamable non-linear interpolation; Post means the post-processing module in the image domain.

TABLE 2.

Performance comparison on the validation set and the test set on *low-dose projections*.

Method	PSNR (val)	SSIM (val)	PSNR (test)	SSIM (test)
FBP	27.40	0.830	29.01	0.880
TV	29.53	0.857	31.62	0.901
FBPConvNet [60]	29.28	0.849	30.72	0.884
RED-CNN [18]	30.60	0.864	32.28	0.902
DeepFBP I	30.73	0.863	32.55	0.905
DeepFBP II	**30.92**	**0.868**	**32.77**	**0.906**

TABLE 3.

Performance comparison on the validation set and the test set on *noisy normal-dose projections.*

Method	PSNR (val)	SSIM (val)	PSNR (test)	SSIM (test)
FBP	16.88	0.632	17.78	0.688
TV	24.17	0.758	25.09	0.801
FBPConvNet [60]	27.03	0.783	27.84	0.815
RED-CNN [18]	27.42	0.803	28.43	0.839
DeepFBP I	27.53	0.809	28.32	0.839
DeepFBP II	**28.07**	**0.815**	**29.11**	**0.849**

TABLE 4.

Performance comparison on the validation set and the test set on *sparse-view low-dose projections*.

Method	PSNR (val)	SSIM (val)	PSNR (test)	SSIM (test)
FBP	21.61	0.709	22.74	0.763
TV	23.79	0.753	24.76	0.800
FBPConvNet [60]	27.21	0.798	28.11	0.838
RED-CNN [18]	27.74	0.807	28.70	0.849
DeepFBP I	28.56	**0.824**	29.79	0.862
DeepFBP II	**28.65**	**0.824**	**29.94**	**0.864**

TABLE 5.

Inference time (MS) in CPU and GPU for images of size 512 × 512.

	CPU (i5–6500)				GPU (RTX2080Ti)			
Method	**Filter**	**Interp**	**Post**	**Total**	**Filter**	**Interp**	**Post**	**Total**
FBP	15.50	353.3	/	368.8	22.00	3.29	/	25.29
TV	/	/	/	1401568.73	/	/	/	28926.24
DeepFBP I	15.28	369.4	1164	1549	38.01	2.78	2.72	43.51
DeepFBP II	15.24	366.5	mi	1493	38.63	2.41	2.93	43.97

Note: Interp means the proposed non-linear interpolation and Post means the post-process module.